

A STELLAR WIND ORIGIN FOR THE G2 CLOUD: THREE-DIMENSIONAL NUMERICAL SIMULATIONS

FABIO DE COLLE, A.C. RAGA, FLAVIO F. CONTRERAS-TORRES, JUAN C. TOLEDO-ROY¹

Submitted to ApJL

ABSTRACT

We present 3D, adaptive mesh refinement simulations of G2, a cloud of gas moving in a highly eccentric orbit towards the galactic center. We assume that G2 originates from a stellar wind interacting with the environment of the Sgr A* black hole. The stellar wind forms a cometary bubble which becomes increasingly elongated as the star approaches periastron. A few months after periastron passage, streams of material begin to accrete on the central black hole with accretion rates $\dot{M} \sim 10^{-8} M_{\odot} \text{ yr}^{-1}$. Predicted Br γ emission maps and position-velocity diagrams show an elongated emission resembling recent observations of G2. A large increase in luminosity is predicted by the emission coming from the shocked wind region during periastron passage. The observations, showing a constant Br γ luminosity, remain puzzling, and are explained here assuming that the emission is dominated by the free-wind region. The observed Br γ luminosity ($\sim 8 \times 10^{30} \text{ erg s}^{-1}$) is reproduced by a model with a $v_w = 50 \text{ km s}^{-1}$ wind velocity and a $10^{-7} M_{\odot} \text{ yr}^{-1}$ mass loss rate if the emission comes from the shocked wind. A faster and less dense wind reproduces the Br γ luminosity if the emission comes from the inner, free wind region. The extended cometary wind bubble, largely destroyed by the tidal interaction with the black hole, reforms a few years after periastron passage. As a result, the Br γ emission is more compact after periastron passage.

Subject headings: accretion, accretion discs - black hole physics - galaxies: active - Galaxy: center

1. INTRODUCTION

The G2 cloud is falling towards the Sgr A* black hole (BH hereafter), and was first detected in Br γ images by Gillessen et al. (2012), with an estimated mass of ~ 3 Earth masses. Its closest approach is estimated to occur in early 2014 (de la Fuente Marcos & de la Fuente Marcos 2013), or mid-March 2014 (Phifer et al. 2013), at a distance of ~ 100 AU from the BH.

Gillessen et al. (2013a,b) show that the cloud has developed an elongated structure. Part of the material might have already gone beyond periastron, as evidenced by the large velocity jump observed in PV diagrams of the extended Br γ emission. This stretching of the cloud (due to the tidal forces of the central BH) will result in an extended cloud/BH interaction, lasting for ~ 1 yr.

Even though the region around the galactic center has been extensively monitored in radio wavelengths (see, e.g., Brunthaler & Falcke 2013; Chandler & Sjouwerman 2014) and in X-rays (see Degenaar et al. 2014), no emission from the G2 cloud has yet been detected. This lack of detection at radio and X-ray wavelengths provides an interesting constraint on theoretical models of the G2 cloud (Narayan et al. 2012; Crumley & Kumar 2013; Sądowski et al. 2013b; Yusef-Zadeh & Wardle 2013; Bartos et al. 2013; de la Fuente Marcos & de la Fuente Marcos 2013).

Two possible scenarios for the G2 cloud have been studied:

- a.* that it is an isolated, ISM cloud with an initial spherical (Gillessen et al. 2012) or shell-like (Meyer & Meyer-Hofmeister 2012; Burkert et al.

2012; Schartmann et al. 2012) density distribution,

- b.* that it is a wind bubble (Scoville & Burkert 2013) or a photo-evaporated proto-planetary disk (Murray-Clay & Loeb 2012; Miralda-Escudé 2012) and therefore has a central (undetected) stellar nucleus.

Scenario *a* has been studied with 2D and 3D hydrodynamic (Schartmann et al. 2012; Burkert et al. 2012; Anninos et al. 2012; Abarca et al. 2013; Saitoh et al. 2012; Abarca et al. 2013) and magnetohydrodynamic (Sądowski et al. 2013a) simulations, showing the breakup of the cloud close to periastron and the infall of cloud material towards the central BH.

For this scenario to be acceptable, one needs a valid mechanism for the formation of the cloud, which will in principle be disrupted in its first periastron passage. For example, the possible creation of the cloud through the tidal disruption of the outer envelope of a giant star has been discussed by Guillochon et al. (2014).

Scenario *b* (see above) was modeled analytically by Scoville & Burkert (2013). These authors show that a young, low mass star with a mass loss rate $\sim 10^{-7} M_{\odot} \text{ yr}^{-1}$ and a terminal wind velocity $\sim 100 \text{ km s}^{-1}$ would produce a cometary wind bubble with observational properties similar to the G2 cloud. Ballone et al. (2013) present isothermal, axisymmetric simulations of this scenario, under the assumption of a radial orbit. This is a reasonable approximation for the initial approach of the cloud to the BH (as the orbit of G2 is highly elliptical), but is inappropriate for modeling the periastron passage.

This “cometary wind bubble” scenario for the G2 cloud avoids the issue of the cloud origin. In each periastron passage, the wind bubble will be disrupted. Then, at long enough timescales after the periastron passage the wind

fabio@nucleares.unam.mx

¹Instituto de Ciencias Nucleares, Universidad Nacional Autónoma de México, A. P. 70-543 04510 D. F. Mexico

bubble will be regenerated by the continuing stellar wind pushing against the lower density, outer environment.

In the present paper, we discuss 3D simulations of the time-evolution of a stellar wind bow shock, following the passage through the periastron of the G2 cloud orbit. The simulations include a model for the coronal environment around the BH (Yuan et al. 2003), the gravity force of the BH, and a parametrized cooling function. The differences between our simulations and the ones of Ballone et al. (2013) is that our simulations are 3D (instead of axisymmetric) and include a cooling function (instead of using an isothermal approximation).

2. NUMERICAL METHOD AND SETUP

We solve the hydrodynamic (HD) equations using the adaptive mesh refinement code *Mezcal* (De Colle et al. 2012), extensively used to study astrophysical flows (e.g., De Colle & Raga 2006; De Colle et al. 2008, 2012). Our implementation of the HD equations includes the BH's gravitational force, with a $M_{\text{BH}} = 4.31 \times 10^6 M_{\odot}$ BH mass (e.g., Ghez et al. 2008), and a parametrized non-equilibrium cooling function (Biro et al. 1995). We also take into account the effect of UV photons emitted by the massive stars present in the BH environment, by adding a heating term, which has the only effect of keeping the gas temperature above 10^4 K. We assume that the H in the wind is fully ionized.

The exact stratification of the BH environment is uncertain. In this paper, we take a density and pressure radial dependence of the form $\rho_a = 9.5 \times 10^{-22} (10^{16} \text{ cm}/R) \text{ g cm}^{-3}$ and $p_a = GM_{\text{BH}}\rho/R$ (Burkert et al. 2012; Anninos et al. 2012; Ballone et al. 2013; Schartmann et al. 2012), being R the distance from the BH. This stratified medium is convectively unstable. To avoid the development of the instability, Schartmann et al. (2012), Ballone et al. (2013), and Burkert et al. (2012) reset at every timestep the value of the BH environment density to the unperturbed, hydrostatic value. This is the same strategy used in one of our simulations (integrated for 20 yrs, see below). We also run two simulations integrated during 4 yrs and without resetting the BH environment, i.e. properly computing the bow shock dynamics.

We assume that the G2 cloud is originated by the stellar wind (with a mass-loss rate $\dot{M}_w = 10^{-7} M_{\odot} \text{ yr}^{-1}$) ejected by a young star, which is moving in a very eccentric orbit ($e = 0.966$) with a period of 198 yr (Gillessen et al. 2013b) around the super-massive BH. The interaction of the wind with the ambient medium produces a double shock structure, with an internal shock where the free-wind gas is decelerated, and an external shock where the ambient medium is accelerated. The distance from the double shock structure to the center of the star can be estimated from the ram pressure balance between the wind and the ambient medium (in the reference system of the star):

$$r_{\text{sh}} \approx \sqrt{\frac{\dot{M}_w v_w}{4\pi \rho_a v_a^2}} \quad (1)$$

where v_w is the terminal velocity of the stellar wind, ρ_a is the (position dependent) environmental density and v_a is the orbital velocity of the stellar source of the G2 cloud. The stellar wind is imposed in the code by rewriting at

every timestep the values of the density and velocity inside a sphere with radius $0.2 \times r_{\text{sh}}$ (centered on the star) with the free-wind values.

To study the effect of changing the wind velocity and of injecting the wind during different periods, we run three models: a high velocity model with a $v_w = 200 \text{ km s}^{-1}$ wind velocity integrated for 4 yrs, starting 3 yrs before periastron, and two low velocity models with $v_w = 50 \text{ km s}^{-1}$, and durations of 4 (starting 3 yrs before periastron) and 20 yrs (starting 19 yrs before periastron). The density of the wind is calculated as $\rho = \dot{M}_w / (4\pi r^2 v_w)$ (where r is the distance from the star). The pressure is chosen by fixing the temperature of the wind at 10^4 K, and using the ideal gas equation of state. The exact value of the wind temperature is not important as the Mach number is $\gg 1$ in the free-wind region.

The simulations employ 3D Cartesian coordinates, with a volume of physical size extending from $(-8.2 \times 10^{16}, -3 \times 10^{16}, 0) \text{ cm}$ to $(10^{16}, 1.5 \times 10^{16}, 10^{16}) \text{ cm}$ in the simulation lasting 20 yrs, and from $(-2.2 \times 10^{16}, -2 \times 10^{16}, 0) \text{ cm}$ to $(8 \times 10^{15}, 1.5 \times 10^{16}, 5 \times 10^{15}) \text{ cm}$ in the simulations lasting 4 yrs along the x -, y - and z -axes, respectively, sampled by using (184,90,20) and (96,112,16) cells at the coarsest level of refinement respectively. Reflective boundary conditions are used on the $z = 0$ (orbital) plane. The maximum number of levels of refinement is chosen by requiring a minimum of 20 cells in r_{sh} (and is therefore changing with time). As the star approaches periastron, r_{sh} (equation 1) becomes increasingly small and a maximum of 8 levels of refinement are necessary to properly resolve the free-wind region in the simulations lasting 4 yrs, corresponding to a maximum resolution of $2.4 \times 10^{12} \text{ cm}$. To limit the computational time, in the simulation lasting 20 yrs r_{sh} is set as $r_{\text{sh}} = \max(r_{\text{sh}}, 10^{14} \text{ cm})$. The BH is located at the center of the reference system employed in the simulations, and the star moves in the $z = 0$ plane.

3. RESULTS

Figures 1 and 2 show density slices on the orbital plane for integration times $t = -1/-3 \text{ yr}$ (i.e., 1/3 years before periastron), 0.2 yr and 1 yr (after periastron) for the $v_w = 50$ and 200 km s^{-1} simulations:

- in the $t = -1 \text{ yr}$ frames we see that the $v_w = 200 \text{ km s}^{-1}$ model has a cometary wind bubble ~ 2 times the size of the one of the $v_w = 50 \text{ km s}^{-1}$ simulation (as expected from equation 1),
- in the $t = 0.2 \text{ yr}$ time frames (central column of Figure 3), the two simulations show that the wind bubble has become a broken filament, with a long, trailing tail and a shorter region extending ahead of the position of the stellar wind source,
- in the $t = 1 \text{ yr}$ frames, the region around the BH is filled with a complex distribution of accreting, clumpy structures. The stellar wind is beginning to reform a cometary bubble (seen in the top region of the $v_w = 50$ and 200 km s^{-1} simulations). Also, we see filamentary density structures connecting the regenerated wind bubbles to the region close to the BH,

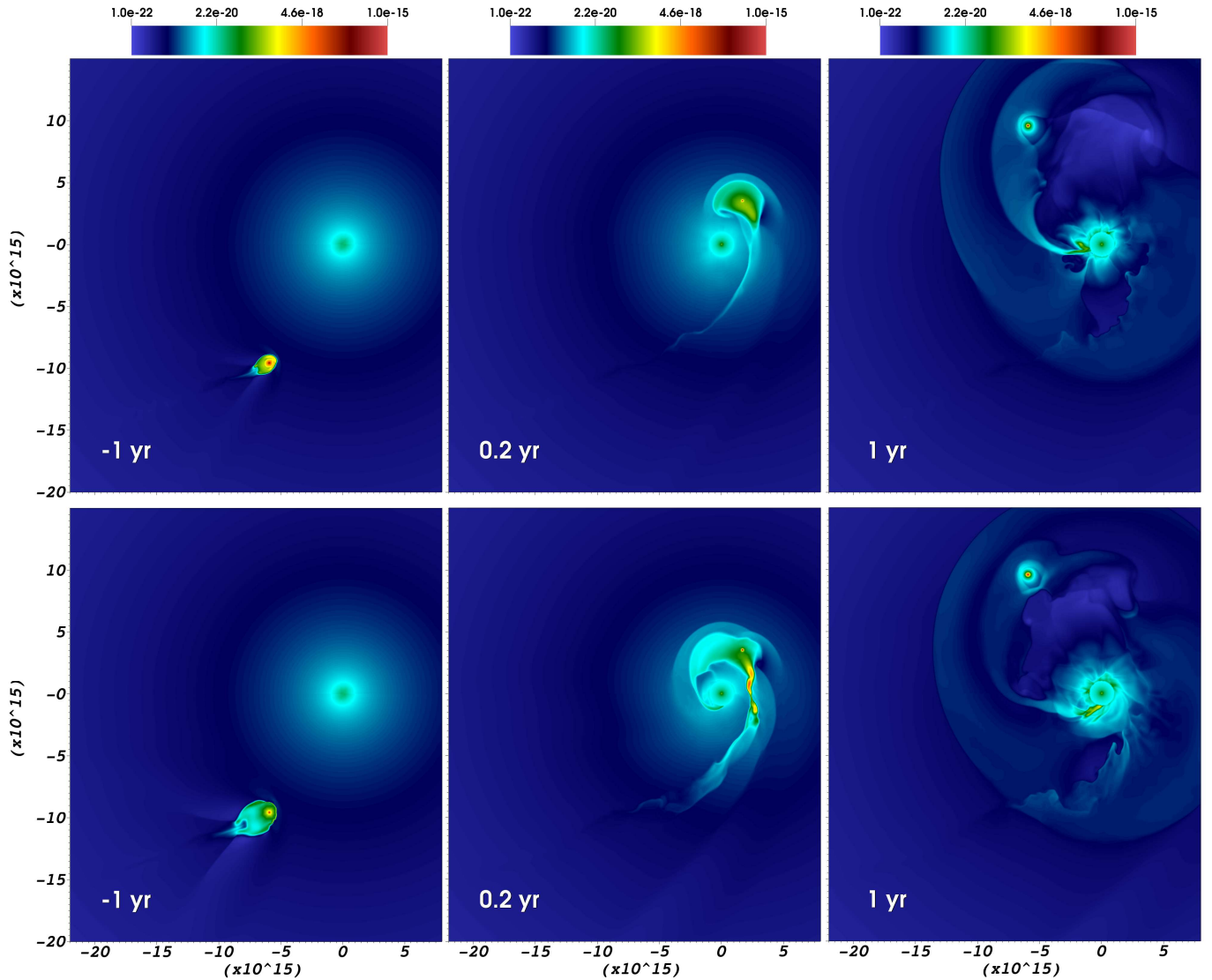


FIG. 1.— Density stratification for the $v_w = 50 \text{ km s}^{-1}$ (top) and $v_w = 200 \text{ km s}^{-1}$ (bottom) models (starting 3 yrs before periastron), for times 1 yr before periastron (left panels), and 0.2 and 1 yr after periastron (central and right panels respectively). The plot corresponds to a cut of the three-dimensional box along the $z = 0$ plane. The BH is located at the origin of the coordinate system.

- Figure 2 shows the effect obtained by considering a wind injected during a much longer timescale. Wind material accumulates around the central star, while a low density, extended tail forms behind the cometary wind bubble which is also more extended in volume before periastron.

Figure 3 shows a composition of the predicted $\text{Br}\gamma$ intensity maps for different evolutionary times and a position-velocity diagram for the 20 yrs, $v_w = 50 \text{ km s}^{-1}$ simulation. The $\text{Br}\gamma$ emission coefficient is obtained by solving a 15 energy level recombination cascade problem with the parameters of Brocklehurst (1970). From a fit to the temperature dependence of the $\text{Br}\gamma$ emission we obtain:

$$L_{\text{Br}\gamma} = 9.55 \times 10^{-29} \frac{n_e n_{\text{HII}}}{(T/T_0)^{0.75}} \left(1 - e^{-\left(\frac{T}{T_0}\right)^{-0.74}} \right) \text{ erg s}^{-1}, \quad (2)$$

which reproduces the recombination cascade calculation within 3% in the $T = 10^3 \rightarrow 10^6 \text{ K}$ temperature range.

These intensity maps correspond to the orientation of the G2 cloud orbit given by Phifer et al. (2013). These maps show the evolution of the cloud from a cometary shape (for times $t < -1 \text{ yr}$) to an elongated filament (at $t \sim 0$) and finally to a more compact, centrally peaked emission structure (in the months following periastron passage). A relatively long time, of order $10^{15} \text{ cm} / v_w$ ($\sim 6 \text{ yr}$ for the $v_w = 50 \text{ km s}^{-1}$ model) will be necessary for the cloud to regain the size that it had at $t = -1 \text{ yr}$ before periastron. The $v_w = 50 \text{ km s}^{-1}$ model presents less extended emission at all evolutionary times. The position-velocity diagram (Figure 3) shows an elongated emission extending a few hundred km s^{-1} in the velocity channel, qualitatively similar to the observed one (e.g. Gillessen et al. 2013b), becoming less extended spatially after periastron passage and much more extended in velocity space during and immediately after periastron passage.

Figure 4 shows the spatially integrated $\text{Br}\gamma$ luminosity as a function of time, computed by adding the contri-

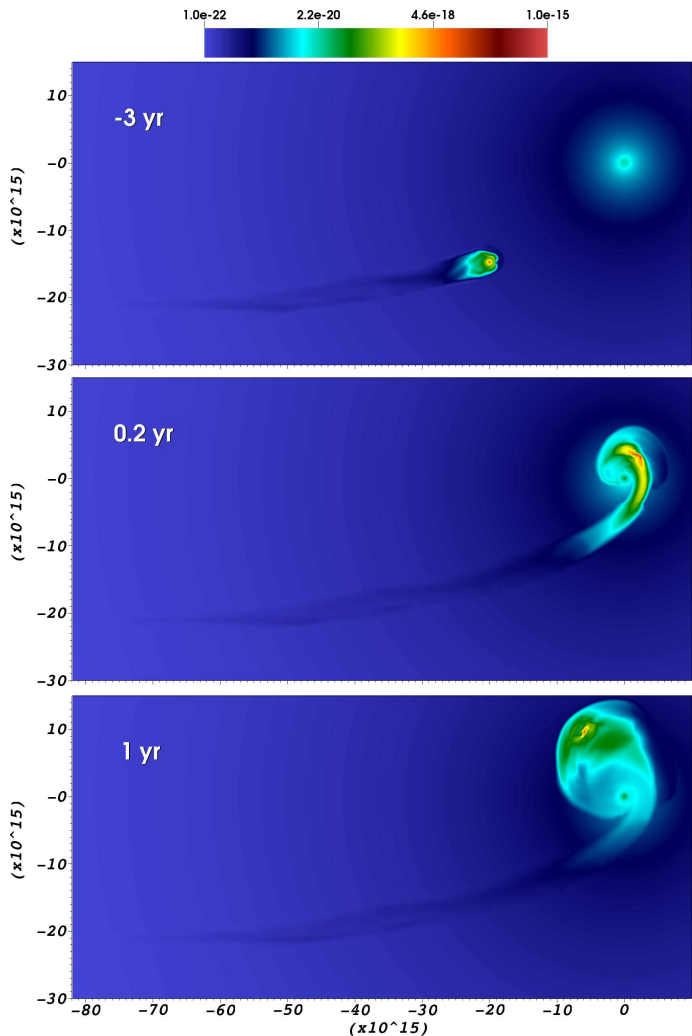


FIG. 2.— The same as in Figure 1, but for a simulation with $v_w = 50 \text{ km s}^{-1}$ starting 19 yrs before periastron.

bution of the cells located at a distance $R \geq R_{\text{sh}}$ from the center of the star, i.e., the shocked wind, and a fixed contribution of 10^{30} - $10^{31} \text{ erg s}^{-1}$ assumed to come from the inner-region of the free-wind, and corresponding to a recombination rate of 10^{42} - 10^{43} s^{-1} respectively. The shocked wind component of the $v_w = 50 \text{ km s}^{-1}$ model shows a larger Br γ luminosity (by a factor ≈ 10) with respect to the $v_w = 200 \text{ km s}^{-1}$ model. Both models present a slow rise during the months/years preceding periastron passage, which is not present when the constant free-wind flux dominates the total luminosity, and a fast decrease during the first month after periastron.

Finally, in Figure 5 we show the mass accretion rate \dot{M}_{BH} for the 20 yrs, $v_w = 50 \text{ km s}^{-1}$ model, computed by tracking the mass density flux across a $R = 10^{15} \text{ cm}$ sphere centered on the BH. \dot{M}_{BH} shows a quick increase during periastron passage, followed by a slow drop of the mass accretion rate after $\approx 0.2 \text{ yr}$, with values of \dot{M}_{BH} of $\sim 3 \times 10^{-8} M_{\odot} \text{ yr}^{-1}$. We can therefore expect that the mass accretion rate will remain large (above $10^{-8} M_{\odot} \text{ yr}^{-1}$) for several years after periastron passage.

4. DISCUSSION

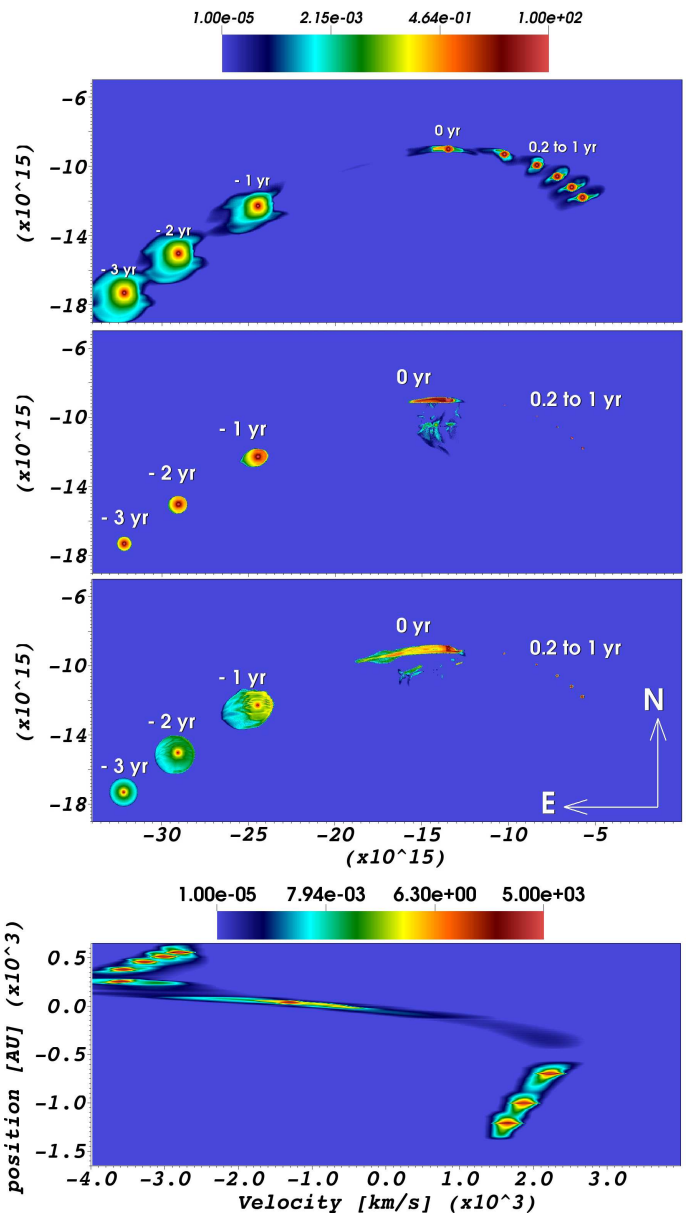


FIG. 3.— *Top panels*: Br γ emission map (in units of $[\text{erg s}^{-1} \text{ cm}^{-2} \text{ sterad}^{-1}]$), projected on the plane of the sky for the (from top to bottom) $v_w = 50 \text{ km s}^{-1}$ (20 and 4 yrs) and $v_w = 200 \text{ km s}^{-1}$ models. *Bottom panel*: Position-Velocity diagram for the $v_w = 50 \text{ km s}^{-1}$, 20 yrs model. The figure includes the emission occurring at different times, with the labels in the top panels indicating the emission time with respect to the periastron passage.

Our 3D simulations of the interaction between a stellar wind and the Sgr A* environment show a complex dynamical behavior. As the star moves towards periastron, a weak forward shock (with Mach number $\lesssim 2$) is formed. Because of the rapid increase in the orbital velocity, the shocked region is unable to adjust to the equilibrium configuration expected from ram-pressure balance (equation 1). As a consequence, the size of the interaction region is larger (smaller) than predicted by equation 1 before (after) periastron passage. At periastron, strong tidal forces and the development of instabilities break the wind bubble, forming an elongated structure with small, dense condensations.

These dense knots accrete onto the central region with

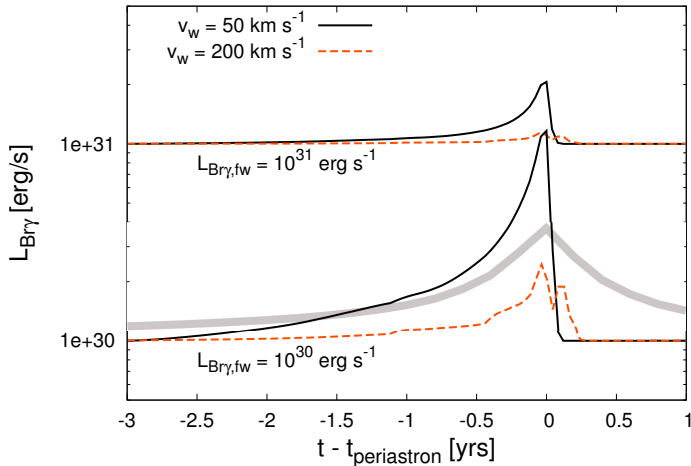


FIG. 4.— Time evolution of the integrated Br γ luminosity, for the $v_w = 50 \text{ km s}^{-1}$, 4 yrs (black, solid line) and 20 yrs (thick, grey line) models, and $v_w = 200 \text{ km s}^{-1}$ (orange, dashed lines) model. The Br γ luminosity is computed by integrating the flux emitted by the shocked wind and by adding a fixed luminosity of $10^{30} \text{ erg s}^{-1}$ (bottom curves) and $10^{31} \text{ erg s}^{-1}$ (upper curves) to simulate the emission coming from the (unresolved in the simulation) inner region of the unshocked wind.

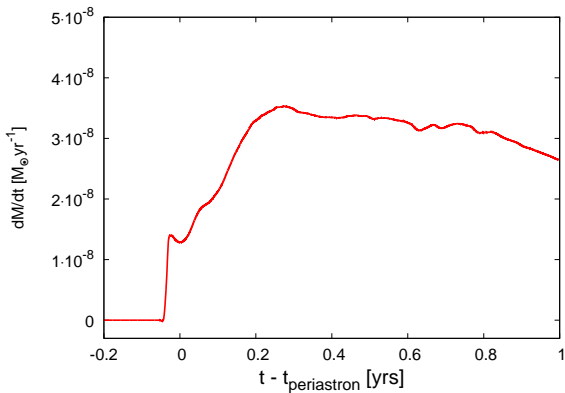


FIG. 5.— Accretion mass rate on the BH (simulated as a free boundary with radius $R = 10^{15} \text{ cm}$) as a function of time for the $v_w = 50 \text{ km s}^{-1}$, 20 yrs simulation.

a \dot{M}_{accr} of $\approx 3 \times 10^{-8} M_{\odot} \text{ yr}^{-1}$ accretion rate (see Figure 5). These values are comparable to those obtained in 3D simulations of the isolated clump scenario (Anninos et al. 2012), and are also of the same order as the accretion rate on the BH inferred from the X-ray Sgr A* luminosity ($\dot{M}_{\text{BH}} \sim 10^{-9} - 10^{-7} M_{\odot} \text{ yr}^{-1}$, see e.g. Aitken et al. 2000). On the other hand, the spherical mass accretion rate (Bondi 1952), computed at the distance from the BH where our value of \dot{M}_{acc} is calculated ($R = 10^{15} \text{ cm}$), is $\dot{M}_B \sim 4 \times 10^{-6} M_{\odot} \text{ yr}^{-1}$ (e.g. Yuan et al. 2003). As the streams of material accreting from G2 onto the inner region of the BH (where the X-ray emission is thought to be generated) depends on not fully understood physical processes (see, e.g., the discussion of Anninos et al. 2012), it is possible that the small \dot{M}_{accr} obtained from the simulations ($\lesssim 0.02 \times \dot{M}_B$) could produce X-ray flares during the upcoming years.

No variations in the emission at radio wavelengths (associated with relativistic electrons accelerated by the G2 forward shock) have yet been detected (e.g.,

Brunthaler & Falcke 2013; Chandler & Sjouwerman 2014). In the scenario of G2 as an isolated ISM cloud, Narayan et al. (2012) (see also Sądowski et al. 2013b) predicted detectable radio emission with a flux \sim ten times the Sgr A* quiescent flux, while, more recently, Shcherbakov (2014) obtained a 30 times lower radio flux (for the same scenario) by assuming a lower size for the radio emitting region.

In the context of a stellar wind model, Crumley & Kumar (2013) have shown that the radio emission decreases with the forward shock size as the star approaches periastron. Our simulations confirm that the forward shock size drops quickly when the star approaches periastron indicating that it is unlikely to produce detectable radio emission. However, a detailed calculation based on the results of numerical simulations is necessary to make a quantitative prediction of the radio emission, as a simple analytical approach fails to describe the elongated, broken shock structure observed during the periastron passage.

Observations of the G2 cloud with the *Integral Field Spectrograph* on the VLT, SINFONI, show a compact Br γ emission from the head of G2 with a luminosity of $\sim 8 \times 10^{30} \text{ erg s}^{-1}$, and an extended tail with approximately the same luminosity (Ballone et al. 2013). Our low-velocity ($v_w = 50 \text{ km s}^{-1}$) simulation does produce a compact emission and an extended tail with comparable Br γ luminosities (see Figure 3).

The Br γ luminosity of the G2 cloud has remained nearly constant (within the statistical errors) during the last ~ 9 yrs (Gillessen et al. 2013b), while in both the stellar wind and the isolated clump one would expect an increase in the flux as ionization of neutral gas should become more efficient approaching periastron (Scoville & Burkert 2013). In our simulations, both the gas in the free-wind region and the shocked stellar wind material contribute to the Br γ emission. The emission from the shocked ambient medium gas is negligible as it is too hot and rarefied to emit efficiently at infrared wavelengths.

Figure 4 shows that the emission from the shocked stellar wind increases approaching periastron (in agreement with Ballone et al. 2013). The interpretation of the observation remains therefore puzzling. To explain it, we assume the presence of a strong ambient photoionizing radiative field (resulting in a strong Br γ emission from the free wind region), larger than the variability obtained from the simulations in the total Br γ luminosity. A solution to this problem, requiring detailed modeling of the BH environment including radiation transfer, is beyond the scope of this paper.

Our simulations illustrate the fact that (in the stellar wind bow shock scenario) once the G2 cloud passes through periastron and the tail of dense, ionized gas moves toward the central BH, the Br γ emission becomes less extended and more peaked on the position of the star (see Figure 3).

A caveat in the interpretation of our 3D simulations is that they do not properly resolve the dense, low filling factor gas seen in the axisymmetric simulations of Ballone et al. (2013). Therefore, one might expect that higher Br γ luminosities might be obtained in simulations with higher resolutions. This can be seen e.g. comparing

the Br γ emission of the low velocity models in Figure 4.

Recent observations by Ghez et al. (2014) show that G2 is still intact at periastron passage, indicating that a stellar component is probably present within the G2 cloud. Clearly, the issue of whether or not the G2 cloud is fed by a central, stellar source will be elucidated by observations over the next few months. If there is indeed a stellar component to G2, a compact Br γ source should survive periastron passage and continue its motion along the G2 orbit. This compact source should become more extended over the next few years, as the stellar wind bow shock develops again.

The simulations presented in this paper are a first attempt at modelling the destruction of a stellar wind bubble on passage through the G2 periastron. In about a

~ 1 yr timescale, once observations of the periastron passage clarify the origin of the G2 cloud, it might become worthwhile to pursue more detailed models, e.g., including the rotation of the BH environment (Abarca et al. 2013) and/or the transfer of ionizing radiation.

We acknowledge P. Crumley, D. González-Casanova, J. Guillochon, L.F. Rodriguez for helpful discussions. This research was supported by the DGAPA-PAPIIT-UNAM grants IA101413-2, IG100214, IN105312, IN106212, and the CONACyT grants 101356, 101975, 165584, 167611 and 167625. FFC-T acknowledges ICN-UNAM for supporting his postdoctoral stay.

REFERENCES

- Abarca, D., Sadowski, A., & Sironi, L. 2013, arXiv:1309.2313
 Aitken, D. K., Greaves, J., Chrysostomou, A., et al. 2000, *ApJ*, 534, L173
 Anninos, P., Fragile, P. C., Wilson, J., & Murray, S. D. 2012, *ApJ*, 759, 132
 Ballone, A., Schartmann, M., Burkert, A., et al. 2013, *ApJ*, 776, 13
 Bartos, I., Haiman, Z., Kocsis, B., & Márka, S. 2013, *Physical Review Letters*, 110, 221102
 Biro, S., Raga, A. C., & Canto, J. 1995, *MNRAS*, 275, 557
 Bondi, H. 1952, *MNRAS*, 112, 195
 Brocklehurst, M. 1970, *MNRAS*, 148, 417
 Brunthaler, A., & Falcke, H. 2013, *The Astronomer's Telegram*, 5159, 1
 Burkert, A., Schartmann, M., Alig, C., et al. 2012, *ApJ*, 750, 58
 Chandler, C. J., Sjouwerman, L. O. 2014, *ATel*, 5727
 Crumley, P., & Kumar, P. 2013, *MNRAS*, 436, 1955
 De Colle, F., Granot, J., López-Cámara, D., & Ramirez-Ruiz, E. 2012, *ApJ*, 746, 122
 De Colle, F., Guillochon, J., Naiman, J., & Ramirez-Ruiz, E. 2012, *ApJ*, 760, 103
 De Colle, F., Raga, A. C., & Esquivel, A. 2008, *ApJ*, 689, 302
 De Colle, F., & Raga, A. C. 2006, *A&A*, 449, 1061
 Degenaar, N., Wijnands, R., Reynolds, M T. et al. 2014, *ATel* 5847
 de la Fuente Marcos, R., & de la Fuente Marcos, C. 2013, *MNRAS*, 435, L19
 Ghez, A. M., Salim, S., Weinberg, N. N., et al. 2008, *ApJ*, 689, 1044
 Gillessen, S., Genzel, R., Fritz, T. K., et al. 2012, *Nature*, 481, 51
 Gillessen, S., Genzel, R., Fritz, T. K., et al. 2013a, *ApJ*, 744, 44
 Gillessen, S., Genzel, R., Fritz, T. K., et al. 2013b, *ApJ*, 763, 78
 Guillochon, J., Loeb, A., MacLeod, M., & Ramirez-Ruiz, E. 2014, arXiv:1401.2990
 Meyer, F., & Meyer-Hofmeister, E. 2012, *A&A*, 546, L2
 Miralda-Escudé, J. 2012, *ApJ*, 756, 86
 Mościbrodzka, M., Shiokawa, H., Gammie, C. F., & Dolence, J. C. 2012, *ApJ*, 752, L1
 Murray-Clay, R. A., & Loeb, A. 2012, *Nature Communications*, 3
 Narayan, R., Özel, F., & Sironi, L. 2012, *ApJ*, 757, L20
 Phifer, K., Do, T., Meyer, L., et al. 2013, *ApJ*, 773, L13
 Sądowski, A., Narayan, R., Sironi, L., & Özel, F. 2013a, *MNRAS*, 433, 2165
 Sądowski, A., Sironi, L., Abarca, D., et al. 2013b, *MNRAS*, 432, 478
 Saitoh, T. R., Makino, J., Asaki, Y., et al. 2012, arXiv:1212.0349
 Schartmann, M., Burkert, A., Alig, C., et al. 2012, *ApJ*, 755, 155
 Scoville, N., & Burkert, A. 2013, *ApJ*, 768, 108
 Shcherbakov, R. V. 2013, arXiv:1311.4507
 Shcherbakov, R. V. 2014, *ApJ*, 783, 31
 Yuan, F., Quataert, E., & Narayan, R. 2003, *ApJ*, 598, 301
 Yusef-Zadeh, F., Arendt, R., Bushouse, H., et al. 2012, *ApJ*, 758, L11
 Yusef-Zadeh, F., & Wardle, M. 2013, *ApJ*, 770, L21